J Adv Ceram

Research Article

Ultrasonic-assisted hot pressing (UAHP): A novel strategy to enhance densification and improve the mechanical properties of B_4C

Zhuo Wang[1,†], Jiaojiao Gao[2,†,✉], Jinpeng Song[1,✉], Kuang Sun[3], Xiong Niu[3], Wei Xu[3], Ming Lv[1], Yanchun Zhou[4,✉]

Cite this article: Wang Z, Gao J, Song J, et al. *J Adv Ceram* 2026, **15**(2): 9221236. https://doi.org/10.26599/JAC.2025.9221236

ABSTRACT: Ultrasonic-assisted hot pressing (UAHP) has shown significant potential in enhancing both the densification and mechanical performance of metallic materials. However, the poor high-temperature stability of ultrasonic systems severely limits its application in the fabrication of high-melting-point materials. To fill this gap, UAHP was operated at temperatures exceeding 2000 °C and employed in the preparation of monolithic boron carbide (B_4C) ceramics for the first time. The densification behavior, microstructure evolution, and mechanical properties of B_4C fabricated via UAHP were systematically investigated and compared with those prepared by conventional hot pressing (HP). It was demonstrated that the introduction of high-frequency ultrasonic vibration in UAHP can not only accelerate the densification rate but also reduce the densification temperature and enhance the mechanical properties of B_4C. Specifically, the relative density of B_4C increased from 90.90% to 97.22% at 1900 °C under UAHP, which was comparable to that achieved by HP at 1950 °C, indicating a 50 °C reduction in densification temperature. In addition, a significant increase in densification efficiency by reducing the densification time during UAHP endowed B_4C with both near-full density and superior mechanical properties. The B_4C ceramics prepared by UAHP at 1950 °C for 20 min and at 2050 °C for 5 min exhibited flexural strengths of 669.3±19.4 and 688.3±32.5 MPa, respectively, and fracture toughnesses of 4.37±0.23 and 4.22±0.29 MPa·m$^{1/2}$, respectively. These results suggest that UAHP is a promising strategy for efficient densification and optimization of the mechanical properties of B_4C ceramic and opens a new avenue for the preparation of difficult sintering ceramics.

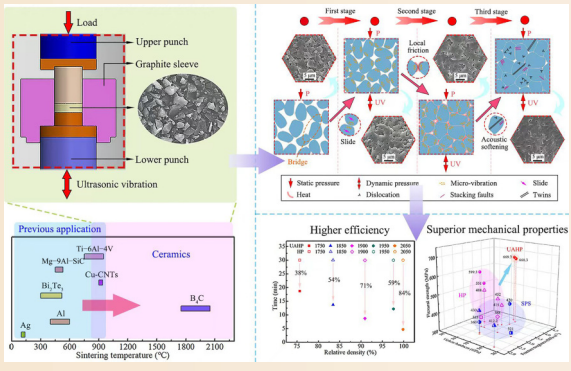

KEYWORDS: ultrasonic assisted sintering; hot pressing (HP); boron carbide (B_4C) ceramics; rapid densification; mechanical properties; toughening mechanism

1 Introduction

Boron carbide (B_4C) has garnered considerable attention due to its unique properties, such as low density, high hardness, high elastic modulus, high melting point, and excellent neutron absorption capability [1–3]. The combination of these characteristics makes it suitable for applications as lightweight armor, high-temperature structural components, cutting tools, wear-resistant components, and neutron radiation shielding materials [4–6].

However, poor sintering ability and low fracture toughness, underpinned by strong covalent bonding and a low self-diffusion coefficient, are the main obstacles that limit its widespread application [7]. To address these issues, metallic additives (such as Ti, Al, and Si) and oxide ceramic additives (such as Al_2O_3, Y_2O_3, and CeO_2) have been introduced into B_4C to lower the densification temperature and enhance sinterability [8–11]. Nevertheless, these additives may result in reduced high-temperature strength and exaggerated grain growth [12–14]. Alternatively, boride and carbide additives can improve the high-temperature strength and enhance the mechanical properties, but effective densification still requires relatively high sintering temperatures [15–17]. In terms of sintering methods, various

† Zhuo Wang and Jiaojiao Gao contributed equally to this work.

[1] College of Mechanical Engineering, Taiyuan University of Technology, Taiyuan 030024, China. [2] College of Aeronautics and Astronautics, Taiyuan University of Technology, Taiyuan 030024, China. [3] Shanghai Chenhua Science Technology Co., Ltd., Shanghai 201804, China. [4] Suzhou National Laboratory, Suzhou 215000, China.

✉ Corresponding authors. E-mail: J. Gao, gaojiaojiao@tyut.edu.cn; J. Song, songjinpeng@tyut.edu.cn; Y. Zhou, yczhou@alum.imr.ac.cn

Received: August 11, 2025; Revised: December 23, 2025; Accepted: December 27, 2025

sintering techniques have been applied to fabricate monolithic B_4C, including pressureless sintering (PS) [18], hot pressing (HP) sintering [19], and spark plasma sintering (SPS) [20]. Although significant achievements in the densification of B_4C have been made using these techniques, ultrahigh sintering temperatures above 2200 °C for PS [21] and prolonged holding times up to 60 min for PS and HP [22,23] are usually needed. In addition, for SPS, inhomogeneous densification may also result, which will influence its mechanical and tribological performance [24].

Dynamic pressure was first introduced in the 1960s in metal powder compaction to improve the green density and shorten the sintering duration [25–27]. Recently, renewed attention has been directed toward extending this approach to the sintering of advanced materials. Based on the vibration frequency, dynamic pressure sintering can be categorized into low-frequency and high-frequency regimes. Low-frequency dynamic pressure sintering, such as hot oscillating press (HOP) sintering with a frequency of 1–50 Hz, has been widely employed for the densification of refractory metals [28–30] and ceramics [31–33], and improved mechanical properties have resulted [34–36]. High-frequency dynamic pressure sintering, such as ultrasonic-assisted hot pressing (UAHP) sintering with a frequency of > 20 kHz, has been utilized for the consolidation of metallic materials, including Al [37], Ti–6Al–4V [38], and Cu [39]. It is noteworthy that not only enhanced densification but also improved mechanical properties have been reported by leveraging the UAHP [40]. However, UAHP is still in its infancy, and its current applications are mainly confined to the low-temperature fabrication of ductile metals, typically processed in the range of 120–950 °C. This limitation stems from the eigenfrequency of the ultrasonic system: As the operating temperature increases, it may exceed the frequency-tracking range of the generator, leading to the ultrasonic system ceasing operation at higher temperatures. To date, although HOP has been extended to the fabrication of refractory metals and ceramics, UAHP has not yet been applied in this domain. Thus, exploring high-frequency dynamic pressure sintering, such as UAHP, for high-temperature ceramics is urgently needed.

It has been generally accepted that the effect of ultrasonic vibration can be broadly categorized into surface effect and volume effect. The surface effect refers to the reduction of interface friction through reducing the true contact surface, lowering the friction coefficient, altering the friction vector, and inducing thermal softening at the interface [41–43]. During powder compaction, ultrasonic vibration efficiently enhances particle rearrangement, decreases interparticle friction, and reduces the friction between powder and die walls, thereby improving the compact density and material homogeneity [44–46]. The volume effect comprises stress superposition and acoustic softening, both of which contribute to reducing the yield and flow stress of materials under ultrasonic vibration [47–50]. The stress superposition effect describes the reduction in average macroscopic stress under the combined action of static load and cyclic dynamic load, leading to the occurrence of elastic deformation of the material [51]. In contrast, the acoustic softening effect refers to the reduction in lattice resistance, lowering the flow stress at the microscopic level [52], which can reduce the activation energy of dislocation motion, thereby facilitating plastic deformation via dislocation slip and twinning [53]. It should be noted that the acoustic softening effect is distinguished from twin boundary (TB) softening [54], B–B bond softening [55], and post-yield softening [22]. Given these well-established mechanisms, UAHP is deemed to hold promise for enhancing the sintering behavior and improving the mechanical performance of ceramics, especially for difficult-to-sinter ceramics.

Inspired by the efficient densification and enhanced properties achieved in the consolidation of metals by UAHP, we embarked on leveraging this promising technique for the densification of covalently bonded ceramics, such as B_4C. B_4C was selected due to its strong covalent bonding and low diffusion coefficient, which is representative of difficult sintering ceramics. To demonstrate the advantage of UAHP over conventional HP, the densification behavior, microstructure evolution, and mechanical properties of UAHP-sintered B_4C were systematically investigated and compared with those prepared by conventional HP. Based on the densification curves, the optimal holding time for UAHP and HP was determined to further enhance the mechanical performance. This work aims to explore two key aspects: First, whether the UAHP can be extended to ultrahigh temperatures, and second, whether efficient densification can be achieved for difficult-to-sinter ceramics, such as B_4C using UAHP.

2 Experimental

2.1 Raw materials

Commercially available B_4C powder (> 96.6% purity, approximately 1 μm, Dalian Zhengxing Abrasive Co., Ltd., China) was used as the raw material. As shown in Figs. S1(a)–S1(c) in the Electronic Supplementary Material (ESM), the powder exhibits an irregular morphology, primarily consisting of flakes with an average size of 0.87 μm. Trace impurities of C and B_2O_3, probably due to incomplete carbothermal reduction, are inevitably present in the raw powder, as shown in the X-ray diffraction (XRD) pattern in Fig. S1(c) in the ESM. The powder was ball-milled in ethanol using B_4C balls at 150 r/min for 12 h with a ball-to-powder weight ratio of 10 : 1. The ball-milled powder was subsequently dried at 69 °C for 24 h. Finally, the powder was screened with a 200-mesh sieve for sintering. As shown in Figs. S1(d)–S1(f) in the ESM, the particle size is effectively reduced, the distribution of particle size is more concentrated, and no additional impurities are introduced during the milling process.

2.2 UAHP processing

For UAHP sintering of B_4C, the B_4C powder without sintering additive was put into a graphite die with an inner diameter of 35 mm and placed in a UAHP furnace (UHP-5T-H-G-18-MIN, Shanghai Chenhua Science and Technology Co., Ltd., China). The temperature was increased from room temperature to 1750–2050 °C at a rate of 10 °C/min, followed by a holding time of 5–30 min. During the holding stage, ultrasonic vibration with a frequency of 20±0.5 kHz and an amplitude of approximately 11.3 μm was applied to the powder. A constant uniaxial pressure of 40 MPa was applied to the powder throughout the heating and dwelling process. The sintering process was performed under vacuum conditions (< 5×10^{-2} Pa). For comparison, reference samples were prepared using conventional HP under identical conditions but without ultrasonic vibration.

2.3 Characterizations

The particle size distribution of the powder was measured using a laser particle size analyzer (Topsizer, Zhuhai OMEC Instruments Co., Ltd., China). Phase composition and residual stress were analyzed by an XRD (DX-2700BH, Haoyuan Instrument Co., Ltd., China) using Cu Kα radiation. Microstructural characterization was conducted using a scanning electron microscope (SEM; EM-30AX+, COXEM Co., Ltd., Republic of Korea) and a transmission electron microscope (TEM; JEM-F200, JEOL, Japan). The polished sample was electrochemically etched

in a 10 wt.% NaOH solution at 25 V for 10–15 s, and the average grain size was evaluated using the linear intercept method from SEM images. Microcrack length density (L) was quantified from SEM images of polished surfaces using ImageJ software and calculated by Eq. (1). For each specimen, at least five representative regions were analyzed.

$$L = \frac{l}{S} \tag{1}$$

where l is the total microcrack length, and S is the corresponding image area.

The bulk density (ρ_b) and apparent porosity (π_a) of the UAHP- and HP-sintered specimens were measured using the Archimedes method and calculated using Eqs. (2) and (3):

$$\rho_b = \frac{m_1}{m_3 - m_2} \times \rho_w \tag{2}$$

$$\pi_a = \frac{m_3 - m_1}{m_3 - m_2} \times 100 \tag{3}$$

where ρ_w is the density of water, m_1, m_2, and m_3 are the masses of dry, immersed, and soaked test specimens, respectively.

The instantaneous relative density (ρ) and densification rate ($\dot{\varepsilon}$) during the dwelling process were calculated as Eqs. (4) and (5):

$$\rho = \frac{H_f}{H_i}\frac{\rho_b}{\rho_t} \tag{4}$$

$$\dot{\varepsilon} = \frac{1}{\rho}\frac{d\rho}{dt} \tag{5}$$

where ρ_t is the theoretical density, H_i and H_f are the instantaneous and final heights of the sample, respectively. The theoretical density of B_4C was calculated via the Rietveld method using GSAS II software. The height of the sample was obtained from the upper punch displacement. To eliminate the interference caused by the thermal expansion of the graphite punch, blank tests were conducted.

Vickers hardness was measured using a microhardness tester (HXD-1000TMC/LCD, Shanghai Taiming Optical Instrument Co., Ltd., China) under a load of 9.8 N for 15 s. The reported Vickers hardness values represented the average of ten measurements per specimen. Flexural strength and fracture toughness were tested using a universal testing machine (WDW-100, Shanghai Bairuo Test Instrument Co., Ltd., China). The flexural strength was evaluated by the three-point bending method using samples with dimensions of 3 mm × 4 mm × 25 mm. The span was 20 mm, and the loading rate was 0.5 mm/min. The fracture toughness was determined utilizing a single-edge notched beam (SENB) specimen with dimensions of 2 mm × 4 mm × 20 mm. The span was 16 mm, the notch depth was 2 mm, the notch width was 0.15 mm, and the loading rate was 0.05 mm/min. For both flexural strength and fracture toughness tests, at least five specimens were tested for each sintering temperature and holding time, and the average value with standard deviation was reported.

3 Results and discussion

3.1 UAHP sintering

Figure 1(a) presents a schematic of the UAHP sintering furnace. The heating element of the furnace is graphite, which allows the realization of a furnace temperature over 2000 °C. The ultrasonic vibration system consists of an ultrasonic generator (V9.0, Hangzhou Success Ultrasonic Equipment Co., Ltd., China; tracking frequency of 20±0.5 kHz), an ultrasonic transducer (YP-5020-4Z, Hangzhou Success Ultrasonic Equipment Co., Ltd., China), and a horn. During UAHP, the ultrasonic transducer is activated by an ultrasonic generator and generates high-frequency (approximately 20 kHz) vibration. The vibration is then

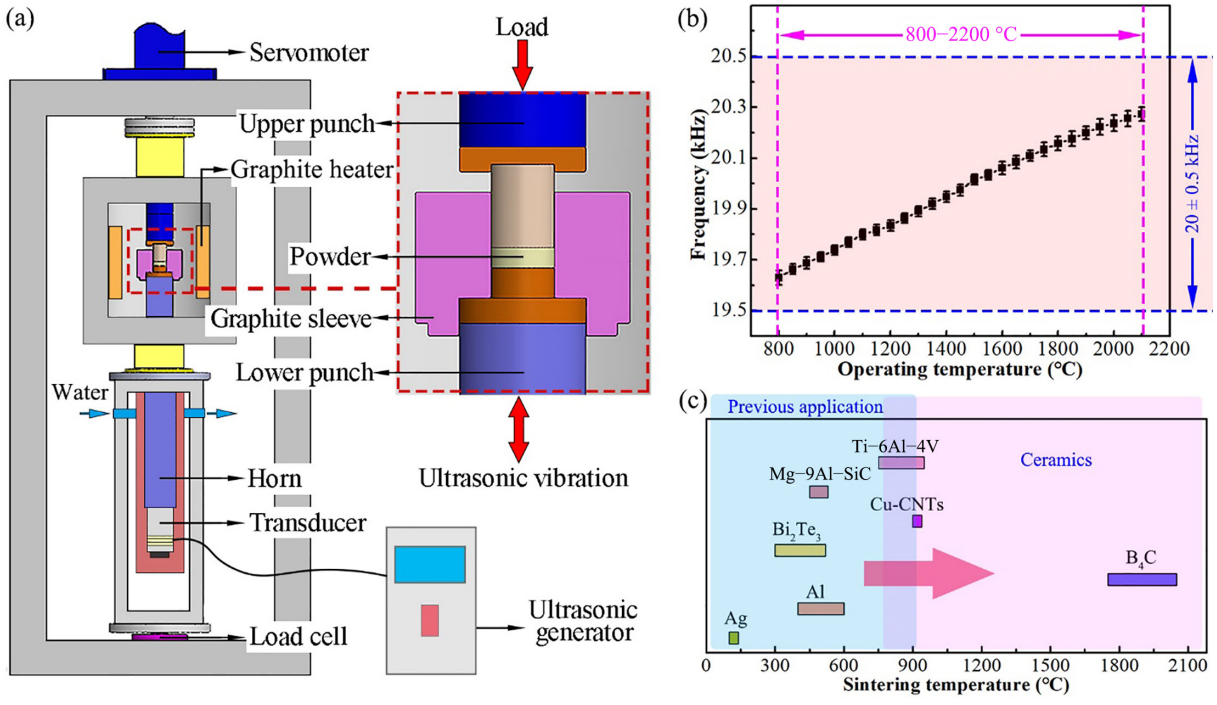

Fig. 1 (a) Schematic of UAHP sintering furnace, (b) corresponding eigenfrequency of UAHP at different operating temperatures, and (c) illustration of leap of operating temperature from fabrication of metals (Ag [56], Bi_2Te_3 [57], Al [37], Mg–9Al–SiC [58], Ti–6Al–4 V [38,40], Cu-carbon nano tubes (CNTs) [39]) to difficult sintering ceramics using UAHP.

transmitted to the powder through a horn. Finally, the powder is sintered under the combined effects of elevated temperature, axial compressive pressure, and ultrasonic vibration. The ultrasonic transducer and the horn are cooled by water to enable stable operation of the ultrasonic system at high operating temperatures.

An *in situ* eigenfrequency measurement was conducted. Under an axial pressure of 40 MPa, the eigenfrequency of the ultrasonic system was measured using B_4C as the sintered material at an operating temperature range of 800–2200 °C in 50 °C increments for 10 min. As the operating temperature increases from 800 to 2200 °C, the eigenfrequency of ultrasonic vibration gradually increases and remains within the frequency-tracking range of 20±0.5 kHz, as shown in Fig. 1(b). These unique combinations ensure that the UAHP sintering furnace can meet the requirements for the efficient fabrication of difficult sintering materials. In Fig. 1(c), we demonstrate the leap of the operating temperature from the fabrication of metals to the difficult sintering of covalently bonded ceramics. This temperature leap poses challenges to all of the systems, as shown in Fig. 1(a). From this aspect, the significance of this work cannot be overemphasized.

3.2 Densification behavior

Figure 2(a) presents displacements of the upper punch and shrinkage rates of the samples during the heating stage of the UAHP and HP processes. As the sintering temperature increases, the upper punch gradually moves downward, indicating progressive shrinkage of the samples. During the heating process from 600 to 1900 °C, the displacements and shrinkage rates of the UAHP and HP are nearly identical since ultrasonic vibration was not applied at this stage. After a rapid increase in the shrinkage rate, a sharp decrease in the shrinkage rate is observed after 1600 °C, resulting in the peaks positioned at 1600 °C, as shown in Fig. 2(a). This change in shrinkage rates can be attributed to carbothermal reduction that occurs due to the presence of unreacted B_2O_3 and C in the raw material, as described by Reaction (6) [59]:

$$2\,B_2O_3 + 7\,C = B_4C + 6\,CO \quad (6)$$

This reaction results in significant volume shrinkage, leading to an increase in the shrinkage rate. As B_2O_3 is gradually consumed, the degree of the reaction slows down, resulting in a corresponding reduction in the shrinkage rate. With a further increase in temperature, the shrinkage rate increases again, which can be attributed to the particle fragmentation, rearrangement, and local plastic deformation induced by external stress and elevated temperature [60]. Significantly, during the dwelling stage, the shrinkage rate of the UAHP initially increases rapidly and then decreases, whereas that of the HP decreases gradually, as shown in Fig. 2(b). The maximum shrinkage rate of the UAHP (0.110±0.01 mm/min) is higher than that of the HP (0.074±0.02 mm/min). At the end of the sintering process, the total displacement under the UAHP reaches 2.96±0.02 mm, which is 6.86% higher than that under the HP (2.77±0.01 mm). This demonstrates that ultrasonic vibration effectively enhances the volume shrinkage of B_4C during the dwelling process.

To further investigate the effect of ultrasonic vibration on the densification process, the relative density, apparent porosity, and average grain size of B_4C sintered by UAHP and HP at 1900 °C for different holding times were evaluated, as shown in Fig. 3. At the beginning of the holding time, numerous interconnected pores can be observed in the UAHP and HP samples (Fig. S2 in the ESM), with a relative density of 79.15% and an average grain size of approximately 1.04 μm. As the holding time increases, the relative density gradually increases, accompanied by a reduction in apparent porosity and progressive grain growth, as shown in Figs. 3(a) and 3(b). Notably, at identical holding times, the relative density (apparent porosity) of bulk ceramics sintered by UAHP is consistently higher (lower) than that prepared by HP. For example, at 15 min, the apparent porosity under UAHP (1.10%) is significantly lower than that under HP (13.77%). The extremely low apparent porosity of the UAHP-prepared bulk is a significant indication that ultrasonic vibration can accelerate the formation of sintering necks and promote the closure of pores. At 30 min, although the apparent porosity of both specimens reaches nearly identical values, the bulk prepared by UAHP still exhibits a higher relative density. The difference in relative density between the UAHP and HP results from the difference in the internal closed pores. A more compact microstructure is observed in the UAHP-prepared bulk, with a final relative density of 97.22%, whereas large closed pores are evident in the HP specimen, with a final relative density of 90.90%. These results show that ultrasonic vibration can facilitate the closure of interconnected pores and accelerate the densification of B_4C. The polished surfaces of B_4C sintered by UAHP and HP at various holding times are presented in Figs. 3(c)–3(h). It is evident from the SEM images that the

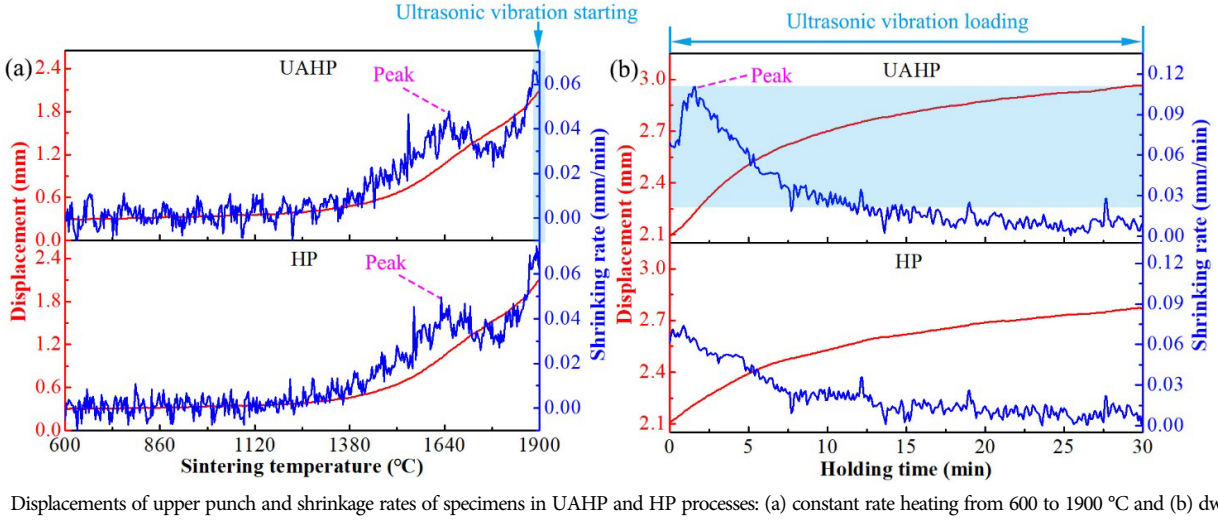

Fig. 2 Displacements of upper punch and shrinkage rates of specimens in UAHP and HP processes: (a) constant rate heating from 600 to 1900 °C and (b) dwelling process at 1900 °C.

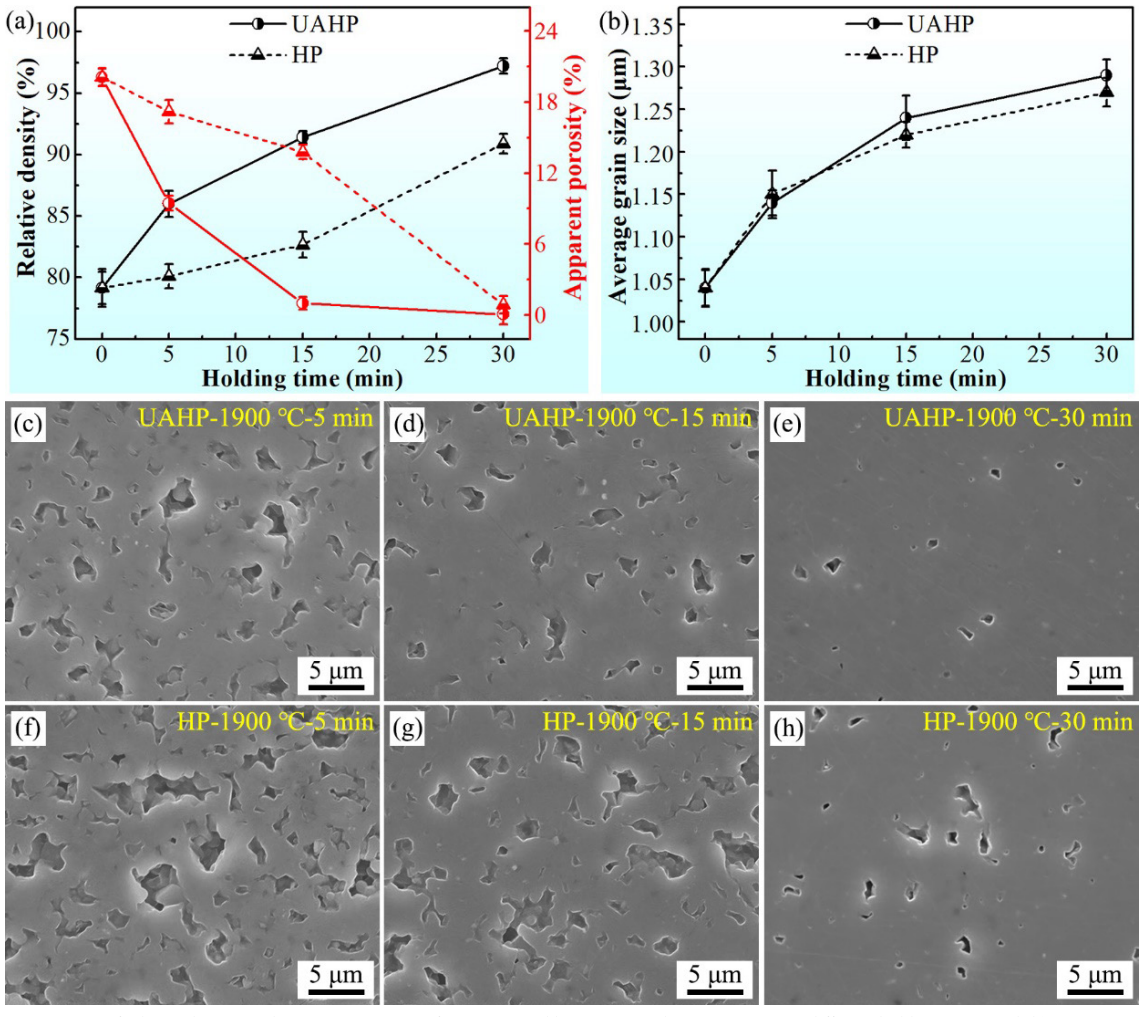

Fig. 3 (a) Comparison of relative density and apparent porosity of B_4C prepared by UAHP and HP at 1900 °C at different holding times and (b) comparison of average grain size of B_4C prepared by UAHP and HP at 1900 °C at different holding times. (c–h) Comparison of polished surface microstructure of B_4C prepared by UAHP and HP at 1900 °C for (c) 5 min UAHP, (d) 15 min UAHP, (e) 30 min UAHP, (f) 5 min HP, (g) 15 min HP, and (h) 30 min HP.

UAHP-prepared B_4C has a higher density and lower porosity at identical holding times. It should be noted that the absolute difference in relative density may be influenced not only by the processing route but also by specimen size and batch size.

To further demonstrate the advantages of UAHP over HP, Fig. 4 compares the isothermal densification and densification rate curves of B_4C sintered by UAHP and HP at various sintering temperatures. As expected, higher sintering temperatures result in higher relative densities, as shown in Fig. 4(a). With prolonged holding time, the relative density increases rapidly in the initial stage, followed by a gradual slowdown or stabilization stage. Throughout the isothermal sintering process, the relative densities of B_4C sintered by UAHP are consistently higher than those sintered by HP under identical holding times. Notably, the B_4C bulk sintered by UAHP at 1900 °C for 30 min achieves a relative density of 97.22%, comparable to that sintered by HP at 1950 °C for 30 min (97.58%), which suggests that the application of ultrasonic vibration enables a reduction in the sintering temperature by approximately 50 °C to achieve near full density. In addition, at an equivalent isothermal sintering temperature, UAHP requires a significantly shorter holding time to achieve the same equivalent final densities of HP (30 min), as evidenced from Fig. 4(b), demonstrating the high sintering efficiency of UAHP. As illustrated in Fig. 4(c), the UAHP demonstrates higher densification rates than the HP at equivalent relative density levels, which is attributed to the surface and volume effects of ultrasonic vibration, which will be discussed in Section 3.4. Overall, these findings confirm that ultrasonic vibration effectively accelerates the densification process, increases the densification rate, and lowers the sintering temperature.

3.3 Phase composition and microstructure

Figure 5 compares the XRD patterns of B_4C sintered by UAHP and HP at various temperatures. Only diffraction peaks corresponding to B_4C (PDF#35-0798) can be detected in these patterns. Impurities C and B_2O_3 are not detected in monolithic B_4C, which can be attributed to the evaporation of low-melting-point B_2O_3 and the reduction reaction between C and B_2O_3 during the sintering process. However, for both UAHP- and HP-prepared materials, all diffraction peak positions shift to low angles with increasing temperature, which can be attributed to the change in the B : C ratio in B_4C with temperature. As we have mentioned in the prior section, during the high-temperature heating process, carbothermal reduction occurs following Reaction (6). An increase in B or a decrease in C may result in an increase in lattice constants, which will be reflected by the shift of peak positions to low angles [55]. Additionally, broadening of the diffraction peaks is observed in the XRD pattern, which can be attributed to the increase in B content [61] or the presence of planar defects, such as twins and stacking faults (SFs) [62,63].

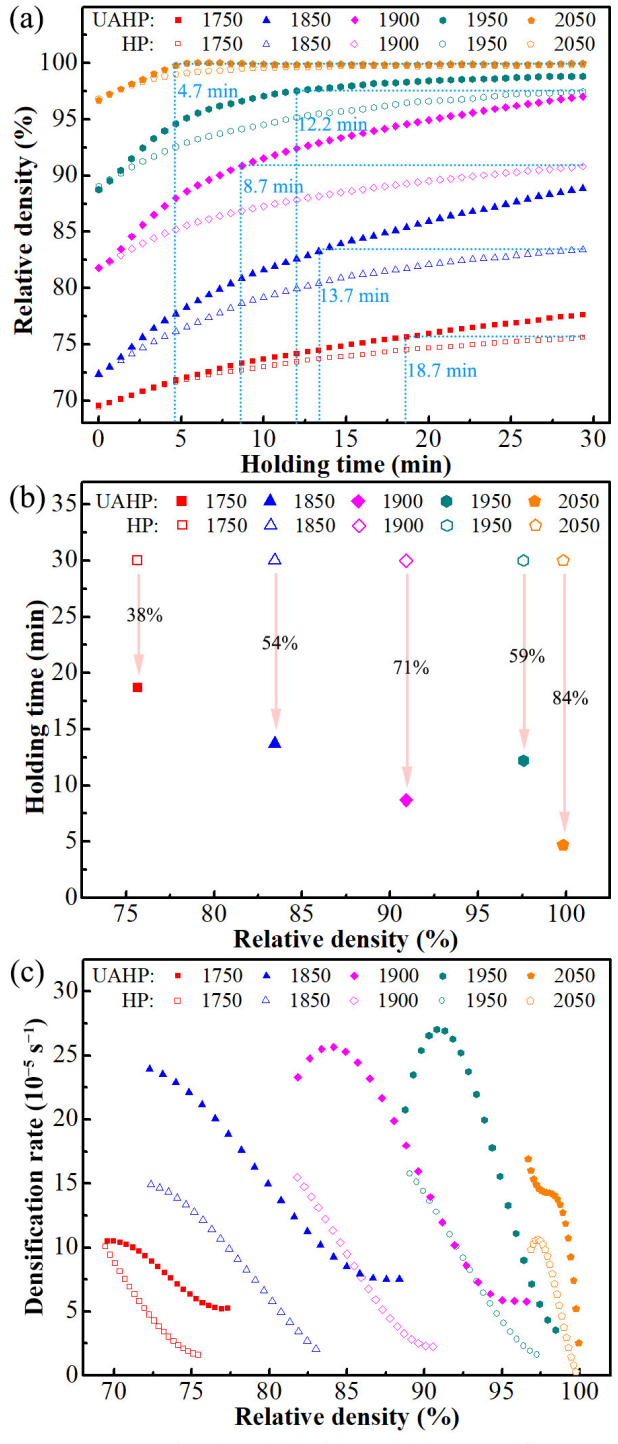

Fig. 4 Comparison of isothermal densification, holding time difference, and densification rate curves of B_4C sintered by UAHP and HP at different temperatures: (a) densification curves, (b) holding time difference to achieve same relative density, and (c) densification rate curves.

Figure 6 presents the etched surfaces of B_4C sintered by UAHP and HP at various temperatures for 30 min. At 1750 °C, UAHP-sintered B_4C exhibits a compact particle arrangement with more sintering necks, whereas HP-sintered B_4C presents a relatively loose structure with numerous interconnected pores, as shown in Figs. 6(a) and 6(d). This suggests that ultrasonic vibration can enhance particle rearrangement by reducing interparticle friction, thereby promoting the formation of sintering necks. In addition, some tiny particles are observed in Fig. 6(a), marked by red arrows, which can be ascribed to particle cusp and edge breakage caused by the high-frequency shear force induced by ultrasonic vibration. With increasing sintering temperature, interconnected pores are progressively closed, accompanied by grain growth. When the sintering temperature exceeds 1900 °C, the B_4C grains sintered by both UAHP and HP grow obviously. The relative porosity and average grain size of B_4C sintered by UAHP and HP are presented in Fig. S3 in the ESM. At 2050 °C, coarse grains are observed in Figs. 6(c) and 6(f), which may deteriorate the mechanical properties. Notably, some lamellar features are presented in B_4C sintered by UAHP at 1900 and 2050 °C and HP at 2050 °C, as indicated by the red square in Figs. 6(b), 6(c), and 6(f). These features can be identified as twins by combining the TEM results presented in Section 3.4.

3.4 Densification mechanisms

The densification mechanism of UAHP in metals is dominated by plastic deformation and creep [40]. However, the mechanisms that underpin the densification of ceramics remain unclear. To gain insight into the densification mechanism, detailed microstructure characterization of B_4C sintered by UAHP at 1900 °C for 30 min by TEM and high-resolution TEM (HRTEM) was carried out. As shown in Fig. 7(a), dislocations, SFs, deformation twins, and residual pores are observed in the low-magnification TEM image. In covalently bonded ceramics such as B_4C, acoustic softening under UAHP does not imply conventional metallic plasticity but rather a transient reduction in lattice resistance to dislocation motion. At elevated temperatures, deformation in B_4C is accommodated through dislocation glide, twinning, and localized amorphization near high-stress regions [64]. The application of ultrasonic vibration superimposes a dynamic acoustic stress field on the static pressure, periodically perturbing the lattice potential and lowering the activation energy for dislocation motion and twin formation [65–67]. The acoustic stress (σ_{UA}) can be written as Eq. (7) [53]:

$$\sigma_{UA} = \sqrt{2}\eta\pi f\rho_t cA \tag{7}$$

where η is an efficiency factor, f is the ultrasonic frequency, c is the sound velocity in the material, and A is the vibration amplitude.

The acoustic stress is related to ultrasonic parameters and material density but not to the type of material. Therefore, acoustic stress is generated in both metals and ceramics. Cyclic shear stress, combined with thermal activation, promotes the activation of localized defects such as dislocations, twins and SFs. Similar defects can be observed in B_4C sintered by HP at 1900 °C for 30 min, as shown in Fig. S4(a) in the ESM. However, compared with the HP-sintered specimen, UAHP-sintered B_4C exhibits a higher density of activated linear and planar defects. This difference could be attributed to the distinct underlying mechanism between UAHP and HP. In the UAHP, the combined effects of high-frequency dynamic shear stress, acoustic softening, and thermal softening collectively promote defect activation, whereas in the HP, these defects primarily arise from static shear stress and thermal softening during densification.

Figures 7(b)–7(f) exhibit the TEM images of SFs and nanoscale twins. Under ultrasonic vibration, part of the local stress at grain boundaries can be released by the nucleation of SFs and nanotwins within grains, as shown in Figs. 7(c) and 7(d). The thickness of the nanotwins is approximately 4–8 nm. The corresponding selected area diffraction pattern (SAED) of the twinning structure reveals that the TBs are parallel to the $(01\bar{1})$ plane, as shown in the inset of Fig. 7(d). In Figs. 7(e) and 7(f), a special region with twins and high-density SFs parallel to the (101)

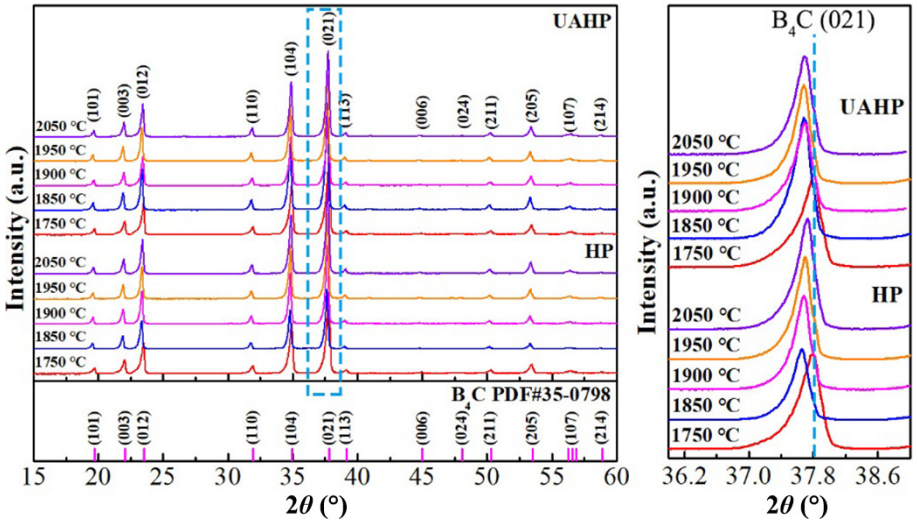

Fig. 5 XRD patterns of B_4C sintered by UAHP and HP at different sintering temperatures for 30 min.

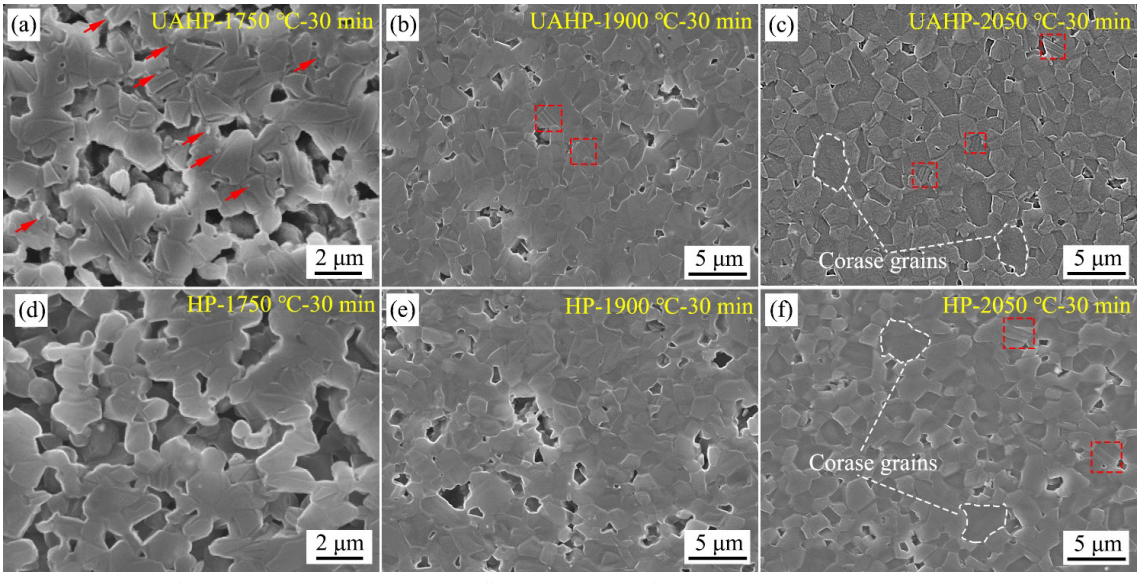

Fig. 6 Etched microstructures of B_4C sintered by UAHP and HP at different temperatures for 30 min: (a) 1750 °C UAHP, (b) 1900 °C UAHP, (c) 2050 °C UAHP, (d) 1750 °C HP, (e) 1900 °C HP, and (f) 2050 °C HP.

plane is shown. The formation of twins and high-density SFs likely originates from local lattice instability caused by shear stress, which facilitates the activation of high-density SFs. Under shear stress, the activated high-density SFs moved forward and formed deformation twins on both sides of the passing area. Similarly, twins and high-density SFs can be observed in HP-sintered B_4C at 1900 °C for 30 min, as shown in Figs. S4(b) and S4(c) in the ESM. The presence of high-density SFs can enhance the local lattice resistance, improving the hardness of B_4C [35]. In Figs. 7(g)–7(i), severe plastic deformation accompanied by the formation of slip bands within the grain interior is shown. Dislocation glide and climb are identified from the HRTEM and inverse fast Fourier transform (IFFT) images of region H1, as shown in Figs. 7(h) and 7(i). These results suggest that the densification mechanism of UAHP-sintered B_4C is dominated by plastic deformation caused by the formation of twins, SFs, and dislocations. It should be noted, however, that the presence of high-density SFs does not always guarantee superior mechanical performance, especially at elevated temperatures where crack initiation at SFs may occur. Therefore, a moderate density and stable configuration of SFs and twins can contribute to strengthening and toughening through crack deflection and dislocation blocking [59,68,69].

Figure 8 presents TEM and HRTEM images and SAED patterns of B_4C sintered by UAHP at 2050 °C for 30 min. As shown in Fig. 8(a), dislocations, deformation twins, SFs, and microcracks are observed in the low-resolution TEM image. Under the combined effects of high temperature and ultrasonic vibration, local stress concentration developed near grain boundaries due to the high-frequency dynamic pressure. Part of this stress was released through the generation of internal defects such as dislocations, SFs, and nanotwins. HRTEM images of nanotwins and high-density SFs are shown in Figs. 8(b) and 8(c). Similar defect structures, particularly SFs and twins, have also been reported in B_4C prepared by HP [55] and SPS [69]. However, in the present UAHP process, these defects are more directly associated with dynamic stress fields induced by ultrasonic vibration, which provides an additional stress-relief pathway. In addition, stress accumulation at grain boundaries results in the formation of microcracks, which can serve as an additional mechanism for stress release [70]. These microcracks can enhance

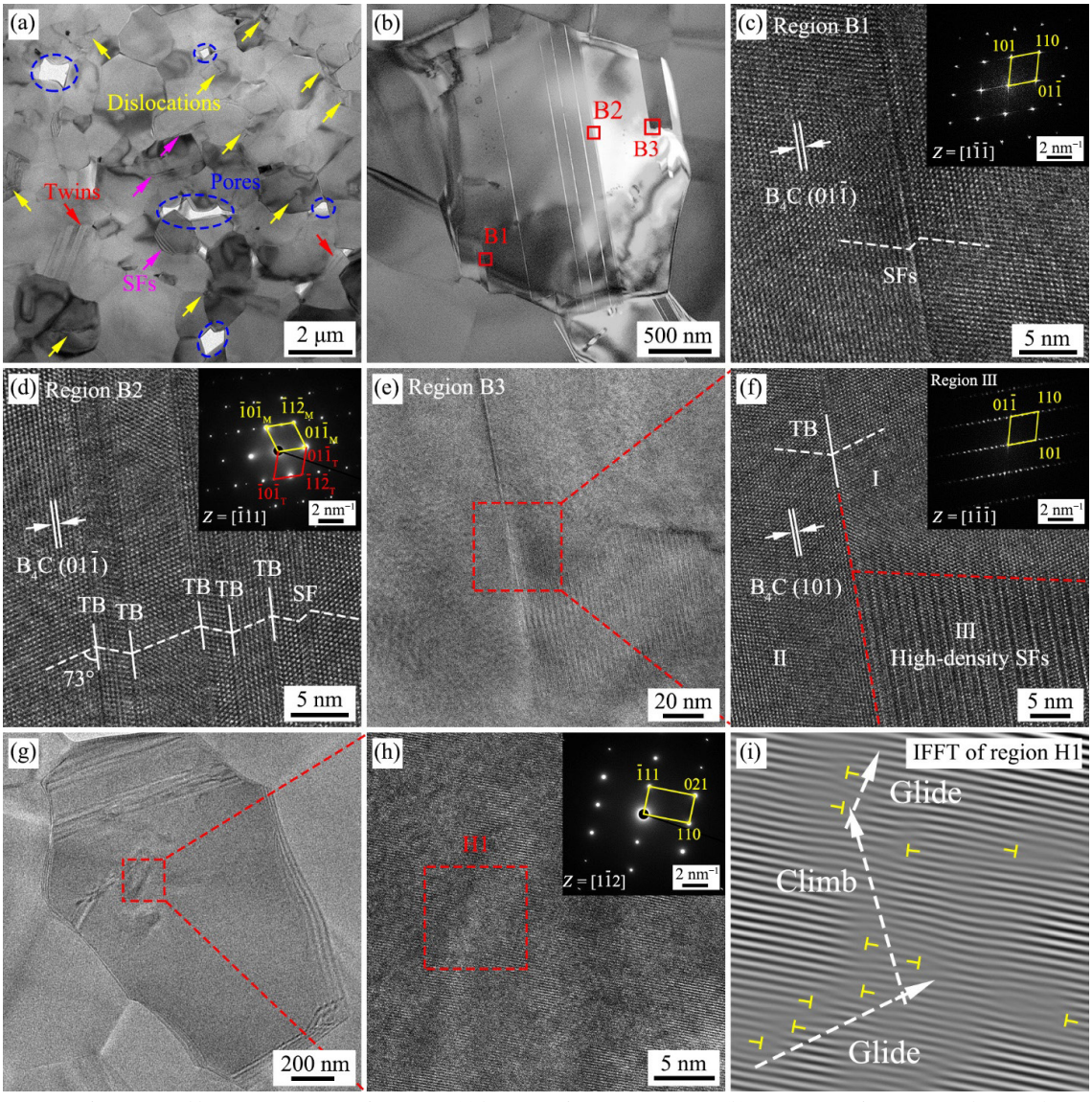

Fig. 7 TEM images of B_4C sintered by UAHP at 1900 °C for 30 min: (a) low-magnification TEM image, (b) TEM image of B_4C grain with SFs and twins marked in regions B1, B2, and B3, (c) HRTEM image from region B1 in (b) and corresponding SAED in $[1\bar{1}\bar{1}]$ zone axis, showing SFs parallel to $(01\bar{1})$ plane. (d) HRTEM image from region B2 in (b) and corresponding SAED pattern in $[\bar{1}11]$ zone axis, showing TBs and SFs are parallel to $(01\bar{1})$ plane. (e, f) HRTEM images of SFs and twins from region B3 in (b), and inset in (f) is SAED in $[1\bar{1}\bar{1}]$ zone axis. TBs and SFs are parallel to (101) plane. (g) TEM image showing deformed region within rectangle and (h) HRTEM image and corresponding SAED in $[1\bar{1}2]$ zone. (i) Dislocation glide and climb drection from region H1 of (h).

the fracture toughness through the microcrack toughening mechanism, which alleviates stress intensity at the crack tip, effectively shielding the crack propagation and increasing the fracture energy [22]. However, they also serve as stress concentrators and potential failure initiation sites, thereby reducing the flexural strength.

Based on the above results, a schematic illustration of the potential densification mechanisms of B_4C sintered by UAHP is presented in Fig. 9. During the UAHP holding stage, ultrasonic vibration with a frequency of approximately 20 kHz and an amplitude of approximately 11.3 μm is applied to the B_4C powder. The primary mechanisms responsible for enhanced densification under ultrasonic vibration include particle rearrangement, local friction heating, acoustic softening, and stress superposition [40,44,71]. At the beginning of the holding time, the green body contains numerous interconnecting pores and a limited number of sintering necks under static pressure.

In the first stage, ultrasonic vibration enhances particle rearrangement by reducing interparticle friction. When ultrasonic vibration is applied to the green body, high-frequency dynamic loading activates microvibration particles, which in turn reduces the actual contact area and causes dynamic friction [37]. The reduced frictional resistance enables particles to undergo rapid sliding, slipping, and rotating. Additionally, the periodic dynamic shear stress induced by stress superposition breaks the weak bonding strength of the sintering neck and then changes from the "bridge" state to the "compact" state [44]. As a result, the particles move to a suitable position, and their gaps are reduced.

In the second stage, ultrasonic vibration facilitates localized friction between contacting particles, generating heat and inducing thermal softening. Based on the frictional heating model [71], the temperature increment (ΔT) caused by local friction heating can be calculated by Eq. (8):

$$\Delta T = \mu\sigma_z A f\sqrt{\frac{\pi t_f}{2\rho^2 Ks}} = \mu\sigma_z A f\sqrt{\frac{\pi t_f}{2Ks}}\frac{1}{\rho} \tag{8}$$

where μ is the effective interparticle friction coefficient, σ_z is the

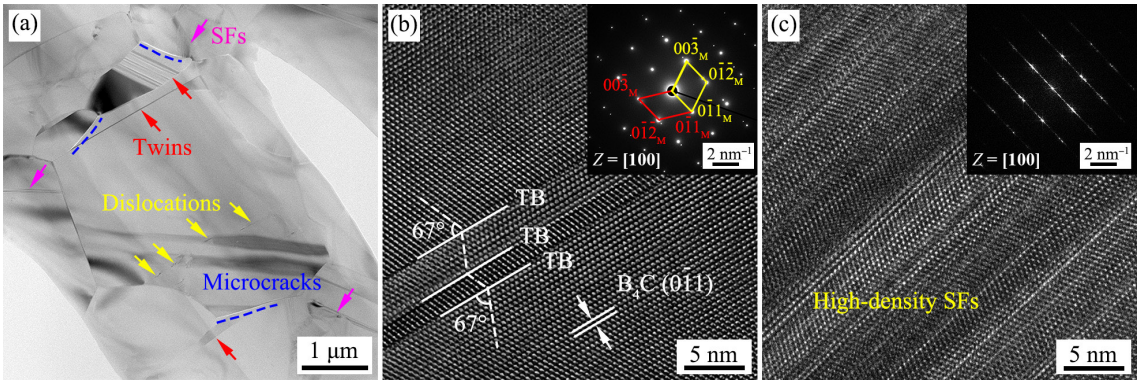

Fig. 8 TEM images of B_4C sintered by UAHP at 2050 °C for 30 min: (a) low-magnification TEM image showing twins, SFs, dislocations, and microcracks. (b) HRTEM image and corresponding SAED pattern in [100] zone axis, nanotwins with their TBs parallel to (0$\bar{1}$1) plane. (c) HRTEM image and corresponding SAED pattern in [100] zone axis; a high density of SFs can be directly seen in the HRTEM image and reflected by faint streaks in SAED pattern inset in the figure.

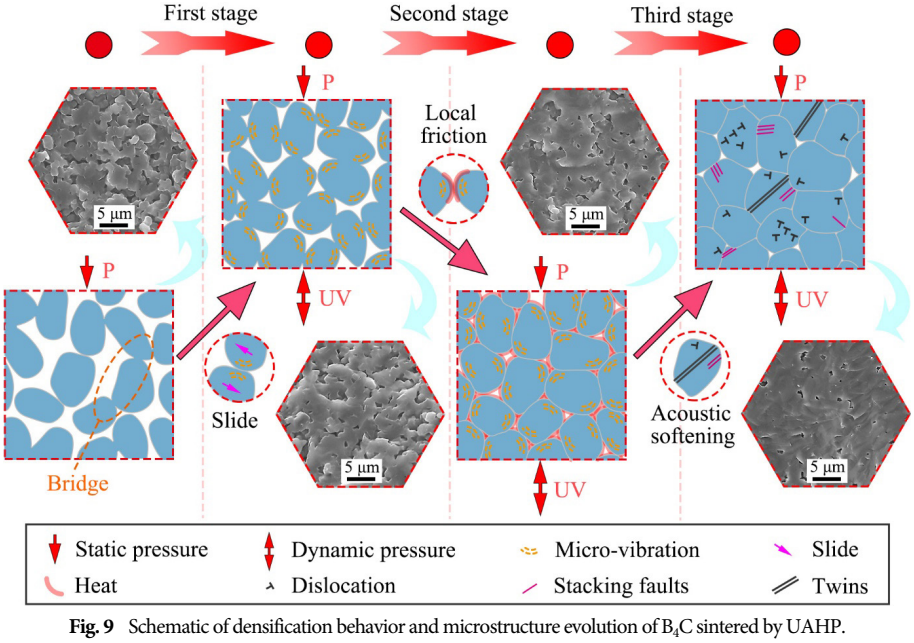

Fig. 9 Schematic of densification behavior and microstructure evolution of B_4C sintered by UAHP.

normal stress, t_f is the duration of vibration interparticle contact, K is the thermal conductivity, s is the volumetric heat capacity, and ρ is the relative density.

At this stage, particles contact discrete points or surfaces, forming an interlocking structure. Under high-frequency dynamic pressure, the particles rub against each other in the discontinuous region to produce local heating [40]. The co-softening effects—thermal-induced softening from external heating and frictional heating, as well as pressure-induced softening from axial pressure and dynamic pressure—synergistically facilitate plastic deformation and accelerate further particle rearrangement. Meanwhile, the accumulation of thermal energy promotes neck growth between particles, contributing to densification.

In the third stage, the dominant mechanism shifts from surface friction-induced heating to a volume effect governed by acoustic softening and stress superposition. When the sintering parameters and sintered material are determined, the corresponding parameters are constant. The ΔT can be simplified as Eq. (9):

$$\Delta T = \frac{C}{\rho} \tag{9}$$

$$C = \mu\sigma_z A f\sqrt{\frac{\pi t_f}{2Ks}} \tag{10}$$

where C is a constant. The temperature increment (ΔT) is negatively correlated with the instantaneous relative density (ρ). With the extension of holding time, ρ gradually increases, while the porosity and discontinuous region decrease, leading to a lower ΔT. Consequently, surface thermal softening induced by interface friction weakens, while internal lattice softening becomes more pronounced. Acoustic softening induced by ultrasonic vibration can lower the lattice resistance and reduce the dislocation activation energy [72]. The activation of intrinsic defects—commonly reported in nonstoichiometric B_4C—is facilitated under ultrasonic vibration during the UAHP process. In addition, the stress superposition of ultrasonic vibration introduces periodic dynamic stress, which can provide an additional driving force for pore shrinkage and elimination. Under the combined effects of acoustic softening and stress superposition, densification is further enhanced during the later stage of sintering. Different sintering methods offer distinct driving forces for densification. For pressure-assisted sintering, complex stress states at particle contacts and neck regions store elastic strain energy, which provides a driving force for densification by mass transport and neck growth [73]. For microwave-assisted sintering, high-frequency electromagnetic fields exert driving forces on mobile ions, thereby enhancing solid-state ionic diffusion [74].

3.5 Mechanical properties

Figure 10 compares the mechanical properties of B_4C sintered by UAHP and HP. With increasing sintering temperature, the Vickers hardness of B_4C gradually increases and eventually reaches a plateau. The hardness of monolithic B_4C is governed by multiple factors, including porosity, grain size, B/C stoichiometry, impurity content, and intragranular deformation, such as dislocations, SFs, and nanotwins [10,13,75]. At lower sintering temperatures, the hardness of monolithic B_4C is primarily influenced by the porosity and grain size. As shown in Fig. S3 in the ESM, UAHP- and HP-sintered B_4C ceramics exhibit comparable grain sizes but differ in porosity levels. A higher relative density corresponds to lower porosity, leading to increased hardness. Therefore, the hardness is mainly governed by the porosity at lower sintering temperatures. At 2050 °C, both UAHP- and HP-sintered B_4C achieve near-full density (99.86% and 99.77%, respectively) and comparable grain sizes but possess different Vickers hardnesses (32.49 and 30.32 GPa, respectively). Under these conditions, the effect of porosity, grain size, and impurity content on the hardness can be excluded. The higher hardness of the UAHP specimens may be attributed to the formation of nanotwins [76]. An *et al.* [77] and Shi *et al.* [78] revealed that nanoscale twins can enhance shear strength through quantum mechanics simulations and molecular dynamics simulations, respectively. The theoretical prediction was further validated experimentally, demonstrating that the hardness of nanotwinned B_4C was approximately 2.3% harder than that of twin-free B_4C [77]. Nevertheless, Li *et al.* [54] reported that the crack preferentially initiated at TBs in B_4C under both indentation and tension loading based on *in situ* observation of fracture behaviors in twinned B_4C crystals. These findings suggest that the hardening and strengthening effect of nanotwins may coexist with potential crack initiation sites.

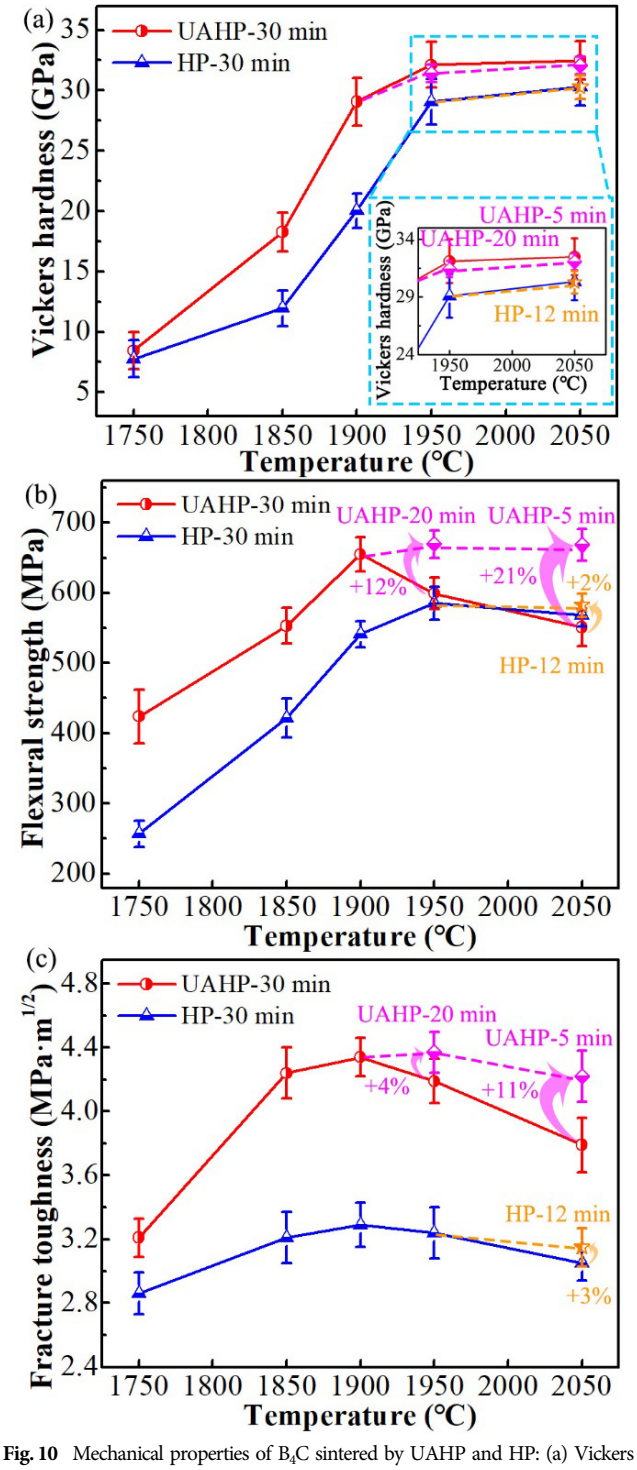

Fig. 10 Mechanical properties of B_4C sintered by UAHP and HP: (a) Vickers hardness, (b) flexural strength, and (c) fracture toughness.

As the sintering temperature increases, the flexural strength and fracture toughness of B_4C initially increase and subsequently decrease. The enhancement in flexural strength is primarily attributed to the reduction in porosity. For UAHP from 1750 to 1900 °C and HP from 1750 to 1950 °C, the decrease in porosity enhances interparticle bonding, thereby improving flexural strength. The correlation between the porosity and flexural strength of B_4C sintered by UAHP and HP for 30 min is shown in Fig. S5 in the ESM. For HP-sintered B_4C, the slight reduction in flexural strength at 2050 °C may be ascribed to grain coarsening. In contrast, when the sintering temperature exceeds 1950 °C, a sharp decline in the flexural strength and fracture toughness is observed in UAHP-sintered B_4C. The drop in flexural strength may be attributed to the formation of microcracks along grain boundaries, as shown in Fig. 8(a). The decline in fracture toughness may be associated with the relaxation of residual compressive stress induced by ultrasonic vibration, which weakens the crack shielding effect during the fracture process [67]. The increased variability in flexural strength and fracture toughness could be attributed to the presence of microcracks in B_4C sintered at 2050 °C for 30 min, which can be reflected in the relatively large error bars. Despite this reduction, UAHP-sintered B_4C still exhibits higher fracture toughness than its HP counterpart. This improvement is ascribed to the presence of microcracks, SFs, and twins in B_4C induced by ultrasonic vibration, which can promote energy dissipation and crack deflection during crack propagation. Due to the limited number of specimens tested in this work, a statistically meaningful Weibull analysis could not be conducted. Future research with large specimen sets will enable a more dependable statistical evaluation of flexural strength.

Figure 11 presents the fracture morphologies of B_4C sintered by UAHP and HP at various temperatures for 30 min. Mixed fracture modes, comprising both transgranular and intergranular fractures, are observed. At 1750 °C, intergranular fracture is predominant, which is attributed to insufficient interparticle bonding strength at lower temperatures. For the UAHP, a compact particle arrangement with well-developed sintering necks is observed in Fig. 11(a), whereas for the HP, a looser microstructure characterized by "bridge" structures is observed in

Figs. 11(d) and 11(e). This difference is attributed to the fact that high-frequency dynamic shear stress induced by ultrasonic vibration can break the "bridge" structures by facilitating particle slip, sliding, and rotation. As the sintering temperature increases, the interconnected pores are gradually closed, and the interparticle bonding strength is enhanced, leading to a higher proportion of transgranular fracture. Typical stepped transgranular fracture features are observed in Figs. 11(b), 11(c), and 11(f). At 1900 °C, a significant distinction in microstructures between UAHP- and HP-sintered specimens is noted: Isolated and closed pores are present in the UAHP-sintered specimen, whereas interconnected pores remain in the HP-sintered specimen, as shown in Figs. 11(b) and 11(e). At 2050 °C, B_4C ceramics sintered by UAHP and HP exhibit a near-fully dense microstructure and exhibit more stepped transgranular fracture. These fracture features can promote crack deflection and dissipate more fracture energy, thereby improving the fracture toughness of B_4C [10].

3.6 Optimization of microstructure and mechanical properties

As demonstrated in the previous sections, extending the holding time can enhance the densification, but with a risk of abnormal grain growth. Therefore, reducing the holding time is an effective strategy for controlling grain growth while achieving high density and superior mechanical performance. As shown in Fig. 4(a), near-fully dense B_4C can be achieved by UAHP at 1950 °C for 20 min and 2050 °C for 5 min and by HP at 2050 °C for 12 min. Table 1 summarizes the relative density and mechanical properties of B_4C sintered under these conditions. Compared with the 30 min holding time, UAHP results in enhancements in the flexural strength of B_4C by 12% and 21% and in the fracture toughness by 4% and 11% at 1950 °C for 20 min and 2050 °C for 5 min, respectively. HP with a reduced holding time (2050 °C for 12 min) yields a 2% improvement in flexural strength and a 3% increase in fracture toughness. Meanwhile, the relative density and Vickers hardness remain almost unchanged, as shown in Fig. 10. These results indicate that shortening the holding time can enable efficient densification while effectively achieving superior flexural strength and fracture toughness. Compared with HP, UAHP exhibits a more pronounced enhancement in flexural strength and fracture toughness under reduced holding time, highlighting the efficiency of ultrasonic vibration in promoting rapid densification and strengthening.

Figure 12 presents the etched and fractured surfaces of B_4C sintered by UAHP under the above mentioned optimized conditions. A uniform grain size distribution and dense microstructures are observed. The average grain sizes of B_4C sintered at 1950 °C for 20 min and 2050 °C for 5 min are 1.30 and 1.38 μm, respectively. Although a shortened holding time effectively mitigates grain coarsening and improves grain uniformity, the degree of grain refinement is limited. Therefore, the primary reason for the enhanced flexural strength and fracture toughness may not be attributed to grain refinement.

To further gain insight, the residual stress in B_4C sintered by UAHP and HP at 2050 °C was evaluated via the $\sin^2\Psi$ method based on XRD with Cu Kα radiation (λ = 1.5406 Å). The diffraction peak of the (303) plane was analyzed. Figure 13(a) shows the $\sin^2\Psi$–d_Ψ plot of B_4C sintered by UAHP at 2050 °C for 5 min. The residual stress (σ_ϕ) was calculated by Eq. (11):

$$\sigma_\phi = \frac{E}{(1+\nu)\sin^2\psi}\frac{d_\psi - d_0}{d_0} \tag{11}$$

where E and ν represent the elastic modulus (E = 450 GPa) [79] and Poisson's ratio (ν = 0.18) [10], respectively; d_Ψ and d_0 represent the measured spacing of the diffracting plane and the spacing without residual stress (d_0 = 1.5004 Å), respectively; and Ψ

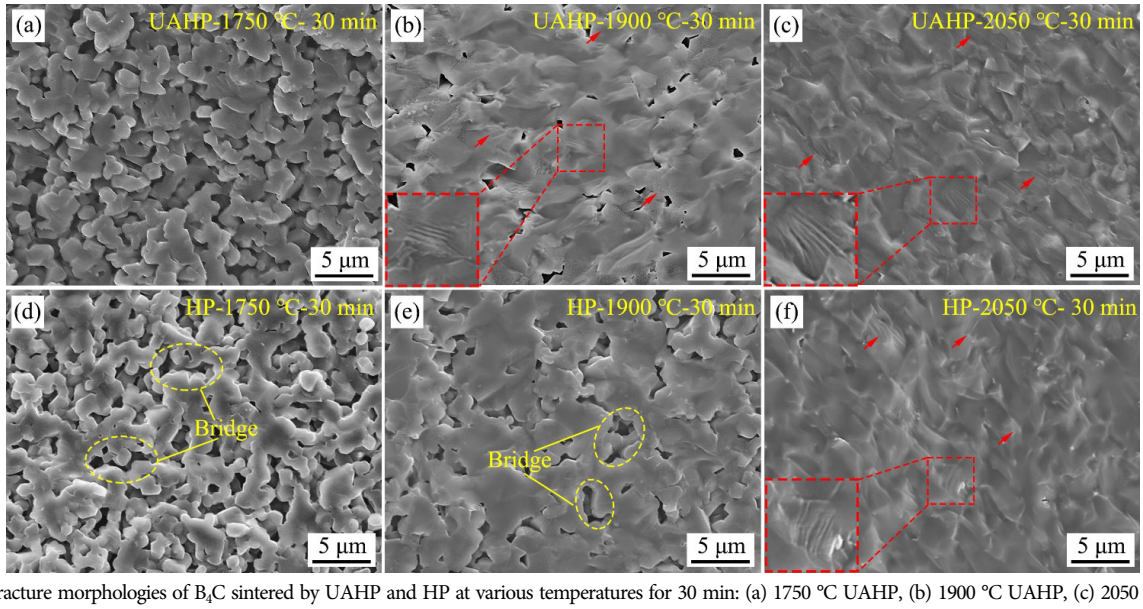

Fig. 11 Fracture morphologies of B_4C sintered by UAHP and HP at various temperatures for 30 min: (a) 1750 °C UAHP, (b) 1900 °C UAHP, (c) 2050 °C UAHP, (d) 1750 °C HP, (e) 1900 °C HP, and (f) 2050 °C HP.

Table 1 Relative density and mechanical properties of B_4C sintered by UAHP and HP after optimizing the holding time

Sample code	Relative density (%)	Flexural strength (MPa)	Fracture toughness (MPa·m$^{1/2}$)	Vickers hardness (GPa)
UAHP-1950 °C-20 min	98.56	669.3±19.4	4.37±0.23	31.42±0.71
UAHP-2050 °C-5 min	99.74	688.3±32.5	4.22±0.29	32.06±0.72
HP-2050 °C-12 min	99.15	582.5±16.7	3.15±0.12	30.27±0.97

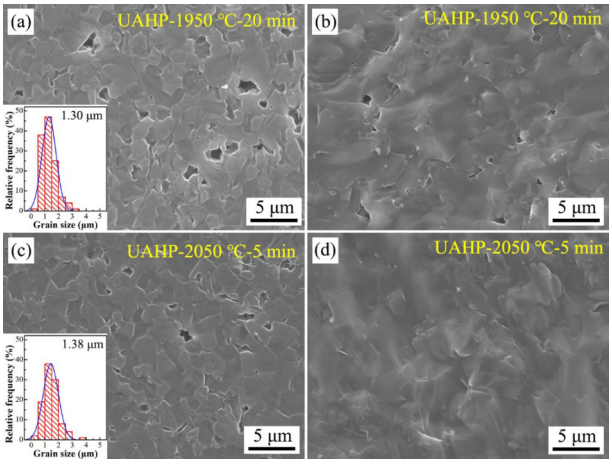

Fig. 12 Etched and fractured surfaces of B_4C sintered by UAHP after optimizing holding time: (a, b) 1950 °C for 20 min and (c, d) 2050 °C for 5 min.

is the tilt angle between the sample normal and the normal of the diffracting plane (Ψ = 0°, 15°, 25°, 35°, and 45°). Negative and positive values correspond to residual compressive and tensile stresses, respectively.

Figure 13(b) presents the evolution of residual stresses of B_4C sintered by UAHP and HP at 2050 °C with different holding times. For UAHP, the residual stress gradually increases from −58.32 MPa at 5 min to 0.25 MPa at 30 min, corresponding to an increase of 58.57 MPa. In contrast, HP-sintered B_4C exhibits slower stress relaxation, increasing from −69.51 to −35.30 MPa over the same holding time with an increase of 30.21 MPa. At a shorter holding time (5 min), UAHP- and HP-sintered B_4C ceramics retain high residual compressive stresses due to insufficient time for local stress release. As the holding time extends, the synergistic effects of thermal and pressure promote atomic diffusion and reduce pore size, leading to a reduction in local stress. Notably, the UAHP exhibits a faster stress relaxation rate than the HP, which can be attributed to the acoustic softening effect of ultrasonic vibration. The acoustic softening effect can reduce the resistance to dislocation motion and facilitate energy dissipation during deformation, combined with thermal and pressure effects [52]. The above analysis demonstrates that ultrasonic vibration can accelerate stress relaxation.

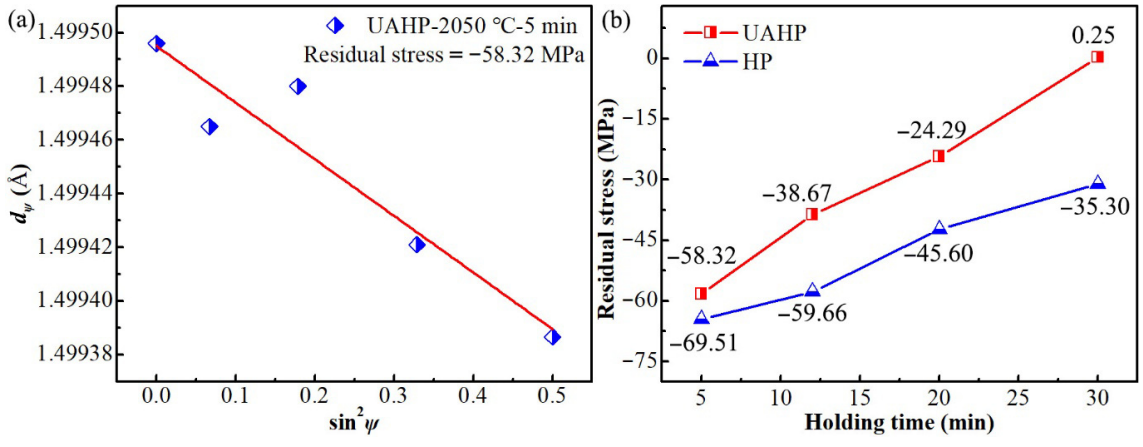

Fig. 13 Residual stress of B_4C calculated by XRD method: (a) $\sin^2\Psi$–d_Ψ plot, (b) residual stresses of B_4C sintered by UAHP and HP at 2050 °C for 5, 12, 20, and 30 min.

For UAHP-sintered B_4C, extending the holding time leads to an increase in the microcrack length density. At 2050 °C, the microcrack length density increases from $(4.29\pm0.4)\times10^{-3}$ μm^{-1} at 5 min to $(9.24\pm2.0)\times10^{-3}$ μm^{-1} at 30 min. This increment reflects the accumulation of microcracks under the combined effects of exposure time and temperature during the UAHP process. It should be noted that the present measurements characterize the final microstructural state. Excessive microcracks may act as preferential crack initiation sites, resulting in a 21% reduction in flexural strength as the holding time increases from 5 to 30 min. Therefore, for UAHP, shortening the holding time can reduce the accumulation of microcracks while retaining beneficial residual compressive stress, thereby improving flexural strength.

Figure 14 shows the crack propagation paths on the polished surfaces of B_4C sintered by UAHP at 2050 °C for 5 and 30 min. In both cases, crack deflection, crack bridging, and crack branching are identified as the primary toughening mechanisms. For B_4C sintered at 2050 °C for 5 min, these mechanisms are mainly associated with residual compressive stress within the material, which suppresses crack propagation and thereby enhances fracture toughness [80]. In contrast, for B_4C sintered at 2050 °C for 30 min, crack deflection, bridging, and branching are predominantly facilitated by deformation twins and SFs induced by ultrasonic vibration [69]. The resulting tortuous crack paths enhance energy dissipation during crack propagation, thus

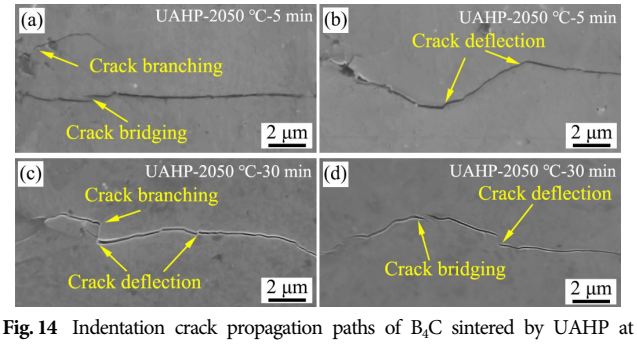

Fig. 14 Indentation crack propagation paths of B_4C sintered by UAHP at 2050 °C for (a, b) 5 min and (c, d) 30 min.

improving fracture toughness. Overall, the relative contributions of these mechanisms vary with holding time, shifting from stress-induced mechanisms at shorter holding times to deformation-induced mechanisms at longer holding times. In addition, crack deflection can be observed in the SENB-tested crack propagation paths for B_4C sintered by UAHP at 2050 °C for 5 and 30 min, as shown in Fig. S6 in the ESM.

4 Conclusions

In this work, UAHP was first employed in fabricating monolithic B_4C ceramics at high operating temperatures exceeding 2000 °C

and compared with conventional HP. The densification behavior, microstructure, and mechanical properties of B_4C were comprehensively investigated. The main conclusions are as follows:

(1) UAHP successfully extends its application from metals to difficult sintering ceramics. This advancement represents a significant breakthrough in expanding the applicability of UAHP to the ceramic field.

(2) Compared with conventional HP, UAHP demonstrates a higher sintering efficiency, achieving near full density at a sintering temperature approximately 50 °C lower and requiring a shorter holding time to reach the equivalent density.

(3) The enhanced densification under UAHP is primarily attributed to three mechanisms: (i) particle rearrangement facilitated by friction reduction, (ii) thermal softening induced by local friction heating, and (iii) acoustic softening coupled with stress superposition, which promotes plastic deformation and accelerates pore shrinkage and elimination.

(4) UAHP can not only increase the sintering efficiency but also improve the mechanical properties. After optimizing the holding time, the B_4C ceramics sintered by UAHP at 1950 °C for 20 min and at 2050 °C for 5 min exhibit excellent mechanical properties compared to those sintered for 30 min at the same temperatures. Specifically, the flexural strength increases to 669.3±19.4 MPa (by 12%) and 668.3±32.5 MPa (by 21%), and the fracture toughness increases to 4.37±0.23 MPa·$m^{1/2}$ (by 4%) and 4.22±0.29 MPa·$m^{1/2}$ (by 11%), respectively.

Despite the leap in operating temperature achieved in this work, the potential and advantages of UAHP still need to be explored, especially in the fields of difficult sintering ceramics and refractory metals. Further investigations are necessary to clarify the densification and grain growth kinetics, to optimize processing parameters and to tailor the properties of diverse materials. Moreover, the current understanding of ultrasonic effects—especially surface and volume effects—has been largely derived from metallic systems. Their applicability and underlying mechanisms in covalently bonded ceramics, such as B_4C, require systematic experimental and theoretical investigation in future work.

Acknowledgements

This work was supported by the National Natural Science Foundation of China (No. 52205492), the Fundamental Research Program of Shanxi Province, China (No. 202303021221037), and the Scientific and Technological Achievements Transformation Guidance Project of Shanxi Province, China (No. 202204021301039).

Availability of data and materials

The data that support the findings of this study are available from the corresponding author upon reasonable request.

Competing interests

The authors have no competing interests to declare that are relevant to the content of this article. The author Yanchun Zhou is the Editor-in-Chief of this journal.

Electronic Supplementary Material

Supplementary material is available in the online version of this article at https://doi.org/10.26599/JAC.2025.9221236.

References

[1] Xu ZW, Zhou XX, Peng K, *et al.* High-performance B_4C–Al_2O_3 composite ceramics fabricated via fast hot-pressing sintering. *Mater Today* 2024, **39**: 108941.

[2] Pan C, Wang AY, Zhang WW, *et al.* Densification of low-density boron carbide by Li doping and its microstructural characterization. *J Am Ceram Soc* 2024, **107**: 5115–5126.

[3] Wang H, Zeng Y, Zhu TB, *et al.* Exceptional strength–toughness–hardness integrated B_4C ceramics with synergistic reinforcement of nano-BN and *in-situ* ceramic phases. *Compos Part B-Eng* 2025, **288**: 111921.

[4] Zhang W, Zhang J. Sliding interface characteristics and self-lubrication mechanism of B_4C–Al_2O_3 composite ceramics. *Tribol Int* 2024, **199**: 110004.

[5] Zhang J, Zhang CH, Zhang S, *et al.* Sliding friction and wear of B_4C ceramics sintered with Al_2O_3/Y_2O_3. *J Eur Ceram Soc* 2024, **44**: 7556–7565.

[6] Zhao J, Xia XJ, Jin X, *et al.* Electrical discharge machinable B_4C–(Zr, Ti)B_2 composites with enhanced mechanical properties. *J Alloys Compd* 2024, **976**: 173260.

[7] Qu ZX, Yu CJ, Wei YT, *et al.* Thermal conductivity of boron carbide under fast neutron irradiation. *J Adv Ceram* 2022, **11**: 482–494.

[8] Kozień D, Czekaj I, Ziąbka M, *et al.* Effect of additives on the reactive sintering of Ti–B_4C composites consolidated by hot pressing and pressureless sintering. *Adv Eng Mater* 2022, **24**: 2101795.

[9] Ayguzer Yasar Z, Koelle MM, Haber RA. Investigation of the effect of impurity of precursor materials on Si-doped boron carbide properties. *Int J Appl Ceram Tec* 2024, **21**: 2263–2272.

[10] Zhang J, Zhang CH, Zhang S, *et al.* Mechanical properties and toughening mechanism of B_4C–Al_2O_3 composite ceramics prepared by hot-press sintering. *Ceram Int* 2024, **50**: 24499–24507.

[11] Jamale S, Venkata Manoj Kumar B. B_4C–SiC composites with tuneable mechanical properties: Role of Al_2O_3–Y_2O_3 sintering additives. *J Alloys Compd* 2024, **976**: 172954.

[12] Lee H, Speyer RF. Pressureless sintering of boron carbide. *J Am Ceram Soc* 2003, **86**: 1468–1473.

[13] Thévenot F. Boron carbide—A comprehensive review. *J Eur Ceram Soc* 1990, **6**: 205–225.

[14] Xu HY, Ji W, Jiang JW, *et al.* Contribution of boundary non-stoichiometry to the lower-temperature plasticity in high-pressure sintered boron carbide. *Nat Commun* 2023, **14**: 4889.

[15] Qiu SH, Zou J, Liu JJ, *et al.* Superhard B_4C-based composites with multifunctionality. *Acta Mater* 2025, **288**: 120817.

[16] Zou L, Li J, Zhou ZH, *et al.* Enhancement of mechanical and tribological properties of hot-pressed B_4C ceramics by CeB_6 addition. *Ceram Int* 2024, **50**: 8340–8351.

[17] Cui Y, Bao SZ, Sun Y, *et al.* Microstructures and mechanical properties of B_4C–TiB_2 ceramics fabricated by reactive sintering using B_4C–Ti mixture. *Ceram Int* 2025, **51**: 30156–30163.

[18] Zhang W, Yamashita S, Kita H. Progress in pressureless sintering of boron carbide ceramics—A review. *Adv Appl Ceram* 2019, **118**: 222–239.

[19] Zhang XR, Zhang ZX, Nie B, *et al.* Microstructure and mechanical properties of fine-grained boron carbide ceramics fabricated by high-pressure hot pressing combined with high-energy ball milling. *Ceram Int* 2018, **44**: 10766–10772.

[20] Zhang M, Yuan TC, Li RD, *et al.* Densification mechanisms and microstructural evolution during spark plasma sintering of boron carbide powders. *Ceram Int* 2018, **44**: 3571–3579.

[21] Wang SF, Hsu YF, Jiang BT, *et al.* Microstructure and mechanical properties of carbon-precursor-added B_4C and B_4C–SiC ceramics subjected to pressureless sintering. *J Eur Ceram Soc* 2023, **43**: 4244–4254.

[22] Zhang YB, Wei J, Li XT, *et al.* Sintering, toughening mechanism and amorphization of B_4C-based ceramic composites: A review. *J Eur Ceram Soc* 2025, **45**: 117075.

[23] Yan QL, Zhou ZH, Yuan TC, *et al.* Effect of micro-doping yttrium oxide on hot-press sintering of boron carbide. *J Cent South Univ* 2023, **30**: 2919–2933.

[24] Zhang XR, Zhang ZX, Wen RL, *et al.* Comparisons of the densification, microstructure and mechanical properties of boron carbide sintered by hot pressing and spark plasma sintering. *Ceram Int* 2018, **44**: 2615–2619.
[25] Lehfeldt E. The effect of ultrasonic vibrations on the compacting of metal powders. *Ultrasonics* 1967, **5**: 219–223.
[26] Naruki K. Vibratory compaction of uranium dioxide, (I): Effect of vibration character. *J Nucl Sci Technol* 1964, **1**: 58–67.
[27] Chachin VN, Sedyako GK. Effects of ultrasonic vibrations on the sintering of metal-powder materials. *Sov Powder Metall Met Ceram* 1968, **7**: 693–694.
[28] Zhao JL, Gao K, Liu DY, *et al.* Sintering process in hot oscillatory pressure of 90W–7Ni–3Fe refractory alloy at different time. *Vacuum* 2022, **195**: 110697.
[29] Gao K, Liu DY, Sun DJ, *et al.* Microstructure and properties of AlCoCrNiFe high-entropy alloy sintered by hot oscillating pressing. *Intermetallics* 2023, **154**: 107802.
[30] Zhu TB, Zhang J, An D, *et al.* Oscillatory pressure sintering: A new method for preparing WC–Co cemented carbides. *J Alloys Compd* 2020, **816**: 152521.
[31] Han Y, Li S, Zhu TB, *et al.* An oscillatory pressure sintering of zirconia powder: Rapid densification with limited grain growth. *J Am Ceram Soc* 2017, **100**: 2774–2780.
[32] Qin XW, Li S, Zhao L, *et al.* Silicon nitride ceramics consolidated by oscillatory pressure sintering. *Ceram Int* 2020, **46**: 14235–14240.
[33] Fan L, Li JH, Huang YB, *et al.* Hot oscillatory pressing of B_4C ceramics for improving densification and mechanical properties. *J Am Ceram Soc* 2022, **105**: 5039–5044.
[34] Zhao K, Zhong WM, Sun MY, *et al.* Sintering mechanism of pure B_4C ceramic prepared by hot oscillating pressing and with excellent mechanical properties. *Adv Eng Mater* 2024, **26**: 2400695.
[35] Hao BQ, Fan L, Li KY, *et al.* Hot oscillatory pressing of SiC ceramics with B_4C and C as sintering additives. *Ceram Int* 2024, **50**: 53628–53634.
[36] Fan L, Song XW, Zhao PF, *et al.* Super strong B_4C ceramics prepared by dynamic sinter forging. *J Eur Ceram Soc* 2023, **43**: 4209–4214.
[37] Abedini R, Abdullah A, Alizadeh Y. Ultrasonic assisted hot metal powder compaction. *Ultrason Sonochem* 2017, **38**: 704–710.
[38] Abedini R, Abdullah A, Alizadeh Y. Ultrasonic hot powder compaction of Ti–6Al–4V. *Ultrason Sonochem* 2017, **37**: 640–647.
[39] Trung TB, Phuong DD, Van Luan N, *et al.* Effect of ultrasonic-assisted compaction on density and hardness of Cu-CNT nanocomposites sintered by capsule-free hot isostatic pressing. *Acta Metall Slovaca* 2017, **23**: 30–36.
[40] Abedini R, Fartashvand V, Abdullah A, *et al.* Evaluation of process parameters and ultrasonic vibration in hot pressing of metal powders. *Mater Sci Eng B-Adv* 2022, **281**: 115731.
[41] Wang XW, Wang CJ, Liu Y, *et al.* An energy based modeling for the acoustic softening effect on the Hall–Petch behavior of pure titanium in ultrasonic vibration assisted micro-tension. *Int J Plasticity* 2021, **136**: 102879.
[42] Zhai JQ, Guan YJ, Li Y, *et al.* The surface effect of ultrasonic vibration in double cup extrusion test. *J Mater Process Tech* 2022, **299**: 117344.
[43] Xie ZD, Guan YJ, Zhu LH, *et al.* Investigations on the surface effect of ultrasonic vibration-assisted 6063 aluminum alloy ring upsetting. *Int J Adv Manuf Tech* 2018, **96**: 4407–4421.
[44] Lv KZ, Yang K, Zhou B, *et al.* The densification and mechanical behaviors of large-diameter polymer-bonded explosives processed by ultrasonic-assisted powder compaction. *Mater Design* 2021, **207**: 109872.
[45] Hwang MH, Lee HS, Han JH, *et al.* Densification mechanism of soft magnetic composites using ultrasonic compaction for motors in EV platforms. *Materials* 2019, **12**: 824.
[46] Fartashvand V, Abdullah A, Ali Sadough Vanini S. Effects of high power ultrasonic vibration on the cold compaction of titanium. *Ultrason Sonochem* 2017, **36**: 155–161.
[47] Li C, Tang XF, Zhang HD, *et al.* Ultrasonic and size effects on the rheological behavior of CoCrFeMnNi high-entropy alloy. *J Alloys Compd* 2022, **913**: 165238.
[48] Hu J, Shimizu T, Yoshino T, *et al.* Ultrasonic dynamic impact effect on deformation of aluminum during micro-compression tests. *J Mater Process Tech* 2018, **258**: 144–154.
[49] Hu J, Shimizu T, Yoshino T, *et al.* Evolution of acoustic softening effect on ultrasonic-assisted micro/meso-compression behavior and microstructure. *Ultrasonics* 2020, **107**: 106107.
[50] Hu J, Shimizu T, Yang M. Investigation on ultrasonic volume effects: Stress superposition, acoustic softening and dynamic impact. *Ultrason Sonochem* 2018, **48**: 240–248.
[51] Zhao YH, Guan YJ, Chen FJ, *et al.* Molecular dynamics study on surface effect in ultrasonic vibration assisted upsetting of monocrystalline copper. *J Mater Process Tech* 2023, **322**: 118189.
[52] Liu Y, Wang CJ, Bi RG. Acoustic residual softening and microstructure evolution of T2 copper foil in ultrasonic vibration assisted micro-tension. *Mat Sci Eng A-Struct* 2022, **841**: 143044.
[53] Kang JR, Liu X, Niezgoda SR. Crystal plasticity modeling of ultrasonic softening effect considering anisotropy in the softening of slip systems. *Int J Plasticity* 2022, **156**: 103343.
[54] Li PH, Bu YQ, Wang LY, *et al. In situ* observation of fracture along twin boundaries in boron carbide. *Adv Mater* 2023, **35**: 2204375.
[55] Tian T, Hu LX, Wang AY, *et al.* Fabrication and characterization of hot-pressed B-rich boron carbide. *Ceram Int* 2022, **48**: 16505–16515.
[56] Wang FL, Nie NT, He H, *et al.* Ultrasonic-assisted sintering of silver nanoparticles for flexible electronics. *J Phys Chem C* 2017, **121**: 28515–28519.
[57] Mei DQ, Wang H, Yao ZH, *et al.* Ultrasonic-assisted hot pressing of Bi_2Te_3-based thermoelectric materials. *Mat Sci Semicon Proc* 2018, **87**: 126–133.
[58] Li M, Wang HX, Nie KB, *et al.* Microstructure and tensile properties of n-SiCp/Mg–9%Al composites prepared by ultrasonic assisted hot pressing of powder. *J Mater Eng Perform* 2017, **26**: 1847–1855.
[59] Li S, Wang HL, Wang HL, *et al.* New insights for strengthening and toughening mechanisms of dislocation in B_4C–ZrB_2–SiC composites using vacuum hot pressing assisted by reaction sintering (VHP-RS). *J Mater Sci* 2023, **58**: 6361–6374.
[60] Du XW, Zhang ZX, Wang Y, *et al.* Hot-pressing kinetics and densification mechanisms of boron carbide. *J Am Ceram Soc* 2015, **98**: 1400–1406.
[61] Mohammad Sharifi E, Karimzadeh F, Enayati MH. Mechanochemical assisted synthesis of B_4C nanoparticles. *Adv Powder Technol* 2011, **22**: 354–358.
[62] Anselmi-Tamburini U, Ohyanagi M, Munir ZA. Modeling studies of the effect of twins on the X-ray diffraction patterns of boron carbide. *Chem Mater* 2004, **16**: 4347–4351.
[63] Xie KY, Domnich V, Farbaniec L, *et al.* Microstructural characterization of boron-rich boron carbide. *Acta Mater* 2017, **136**: 202–214.
[64] Demirskyi D, Sepehri-Amin H, Suzuki TS, *et al.* Ultra-high temperature flexure and strain driven amorphization in polycrystalline boron carbide bulks. *Scripta Mater* 2022, **210**: 114487.
[65] Shao GD, Li HW, Zhan M. A review on ultrasonic-assisted forming: Mechanism, model, and process. *Chin J Mech Eng* 2021, **34**: 99.
[66] Li Z, Li X, Huang ZY, *et al.* Ultrasonic-vibration-enhanced plasticity of an entropic alloy at room temperature. *Acta Mater* 2022, **225**: 117569.
[67] Li QL, Yuan SM, Li Z, *et al.* Mechanical response and microstructure evolution of SiC particle-reinforced Al-MMCs under ultrasonic loading. *Compos Part A-Appl S* 2023, **173**: 107657.
[68] Zhang WW, Cao XC, Zhang JY, *et al.* B_4C-based hard and tough

ceramics densified via spark plasma sintering using a novel Mg_2Si sintering aid. *Ceram Int* 2023, **49**: 145–153.

[69] Liao ZL, He QL, Zhang W, *et al*. B_4C ceramics with increased dislocation density fabricated by reactive spark plasma sintering via carbon nanotubes–boron mixture. *Ceram Int* 2024, **50**: 22443–22455.

[70] Wang D, Zhang YN, Jiao YM, *et al*. Reactive spark plasma sintering of an electrically conductive B_4C–SiC–ZrB_2 composite with enhanced mechanical properties. *J Eur Ceram Soc* 2024, **44**: 2720–2729.

[71] Ward AA, Palmerio NE, Hareland CA, *et al*. Macroscopic yielding and particle-scale densification mechanisms in ultrasonic powder compaction. *J Mech Phys Solids* 2022, **167**: 105011.

[72] Zhou HY, Cui HZ, Qin QH. Influence of ultrasonic vibration on the plasticity of metals during compression process. *J Mater Process Tech* 2018, **251**: 146–159.

[73] Zhao ZP, Zhang XM, Zhang HJ, *et al*. Numerical investigation into pressure-assisted sintering using fully coupled mechano-diffusional phase-field model. *Int J Solids Struct* 2022, **234–235**: 111253.

[74] Booske JH, Cooper RF, Freeman SA, *et al*. Microwave ponderomotive forces in solid-state ionic plasmas. *Phys Plasmas* 1998, **5**: 1664–1670.

[75] Zhou ZH, Zhang M, Yuan TC, *et al*. Effect of impurity on microstructure and properties on hot-pressed boron carbide ceramics. *J Cent South Univ* 2023, **30**: 2441–2457.

[76] Uttam P, Kumar V, Kim KH, *et al*. Nanotwinning: Generation, properties, and application. *Mater Design* 2020, **192**: 108752.

[77] An Q, Goddard WA III, Xie KY, *et al*. Superstrength through nanotwinning. *Nano Lett* 2016, **16**: 7573–7579.

[78] Shi LP, Zhang HC, Ma XL, *et al*. Superhardness in nanotwinned boron carbide: A molecular dynamics study. *Phys Chem Chem Phys* 2023, **25**: 19585–19595.

[79] Wang S, Yang MS, Li HQ, *et al*. High-performance B_4C matrix composites fabricated from the B_4C–Si–CeO_2 system via reactive hot pressing. *Ceram Int* 2022, **48**: 18811–18820.

[80] Guo SQ, Okuma G, Naito K, *et al*. Mechanical behaviours of reactive hot-pressed B_4C-based composites with ZrB_2–ZrC. *J Eur Ceram Soc* 2024, **44**: 116734.